nature physics

ARTICLES

PUBLISHED ONLINE: 7 OCTOBER 2012 | DOI: 10.1038/NPHYS2440

Super-elastic collision of large-scale magnetized plasmoids in the heliosphere

Chenglong Shen[1], Yuming Wang[1]*, Shui Wang[1], Ying Liu[2,3], Rui Liu[1], Angelos Vourlidas[4], Bin Miao[1], Pinzhong Ye[1], Jiajia Liu[1] and Zhenjun Zhou[1]

A super-elastic collision is an unusual process in which some mechanism causes the kinetic energy of the system to increase. Most studies have focused on solid-like objects, and have rarely considered gases or liquids, as the collision of these is primarily a mixing process. However, magnetized plasmoids are different from ordinary gases—as cross-field diffusion is effectively prohibited—but it remains unclear how they behave during a collision. Here we present a comprehensive picture of a unique collision between two coronal mass ejections in the heliosphere, which are the largest magnetized plasmoids erupting from the Sun. Our analysis reveals that these two magnetized plasmoids collided as if they were solid-like objects, with a likelihood of 73% that the collision was super-elastic. The total kinetic energy of the plasmoid system increased by about 6.6% through the collision, significantly influencing its dynamics.

Collisional dynamics is essential in determining the global structure and evolution of macro- and micro- objects, such as planet rings[1], granular materials[2] and nanoclusters[3,4]. To classify collisions in terms of energy transfer, Newton defined the coefficient of restitution, e, which is normally between 0 and 1. However, abnormal e values, such as $e > 1$ (refs 2,5–7) or $e < 0$ (refs 4), have been reported. A super-elastic collision is a process through which the linear kinetic energy of the collisional system increases, that is, $|e| > 1$. In the literature, there have been several mechanisms proposed to explain such an abnormal increase in the linear kinetic energy during a collision. In granular physics, for example, the oblique impact collision with local deformation may help transfer rotational kinetic energy into linear kinetic energy[2,4,5] (hereafter kinetic energy refers to linear kinetic energy). Thermal fluctuations are suggested as another possible reason leading to super-elastic collisions of nanoclusters[3].

In the absence of internal magnetic fields, two encountering plasmoids tend to mix together, just like ordinary gases. However, it is unclear what would happen if they carry strong magnetic fields, especially in regards to the nature of the collision and the energy exchange between them. Coronal mass ejections (CMEs) are large-scale[8] magnetized plasmoids, originating from the solar atmosphere and expanding and propagating into the heliosphere. As they are a frequently occurring phenomenon with an occurrence rate of 4–5 CMEs per day during the solar maximum[9], the encounters and interactions between CMEs are unavoidable. Actually, as a consequence of interactions, multiple-interplanetary-CME structures are often observed by *in situ* instruments[10–14]. Thus, the issue of magnetized plasmoid collision may be addressed by investigating observations of CMEs.

However, the CME dynamics in the heliosphere constitute an intricate problem[15–18], especially when the collision/interaction between CMEs is involved[11,19–22]. The dynamics of two successive CMEs of 24–25 January 2007 was discussed in ref. 21, in which four different scenarios were proposed to explain the observations, one of which is a mysterious collision through which the leading CME gained momentum and finally became faster than the overtaking CME. Most recently, a CME–CME interaction event on 1 August 2010 has been intensively studied with a focus on the CME dynamics, CME-driven shock and radio bursts[22–24]. Numerical simulations of the interaction between CMEs have also been carried out by many researchers[25–32], but few discussed the nature of the CME collisions.

During 2–8 November 2008, the Sun Earth Connection Coronal and Heliospheric Investigation (SECCHI) suites[33] onboard the twin Solar Terrestrial Relations Observatories[34] (STEREO) captured the process of the chasing and colliding of two CMEs in the heliosphere with clear imaging observations. Each SECCHI suite carries the cameras COR1, COR2, HI1 and HI2, and can seamlessly track CMEs from the corona to interplanetary space. As the events occurred near the solar minimum, the conditions in the heliosphere were quite simple. The events provide us with a unique opportunity to study the physical details of CME collisions. As will be seen, the collision between the two CMEs is super-elastic in nature, during which their total kinetic energy increased. These results advance our understanding of the behaviour of large-scale magnetized plasmoids.

Imaging of two successive CMEs and their collision

The two CMEs originated from the Sun at about 00:35 UT and 22:35 UT, respectively, on 2 November 2008, when the STEREO-A spacecraft was located at 0.97 AU and 41° to the west of the Sun–Earth line, and STEREO-B was located at 1.07 AU and 40° to the east (Fig. 1a). These events were reported in ref. 35 with a focus on their solar source locations and *in situ* effects at 1 AU. One can refer to that paper or Supplementary Section S2 for the details of the propagation of the two CMEs in the corona. Here we focus on their collision in the heliosphere.

[1]CAS Key Laboratory of Geospace Environment, Department of Geophysics and Planetary Sciences, University of Science and Technology of China, Hefei 230026, China, [2]Space Sciences Laboratory, University of California, Berkeley, California 94720, USA, [3]State Key Laboratory of Space Weather, National Space Science Center, Chinese Academy of Sciences, Beijing 100190, China, [4]Space Science Division, Naval Research Laboratory, Washington DC 20375, USA. *e-mail: ymwang@ustc.edu.cn.

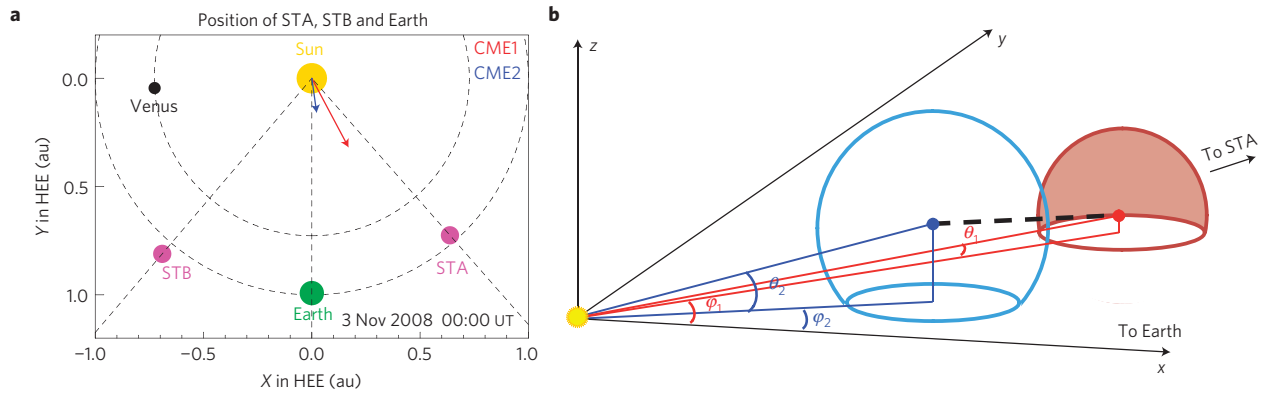

Figure 1 | Configuration of the two CMEs, spacecraft and planets. a,**b**, A sketch map of the positions of the spacecraft (STA, STEREO-A; STB, STEREO-B) in heliocentric Earth ecliptic (HEE) coordinate system (**a**) and the collision of the CMEs (**b**).

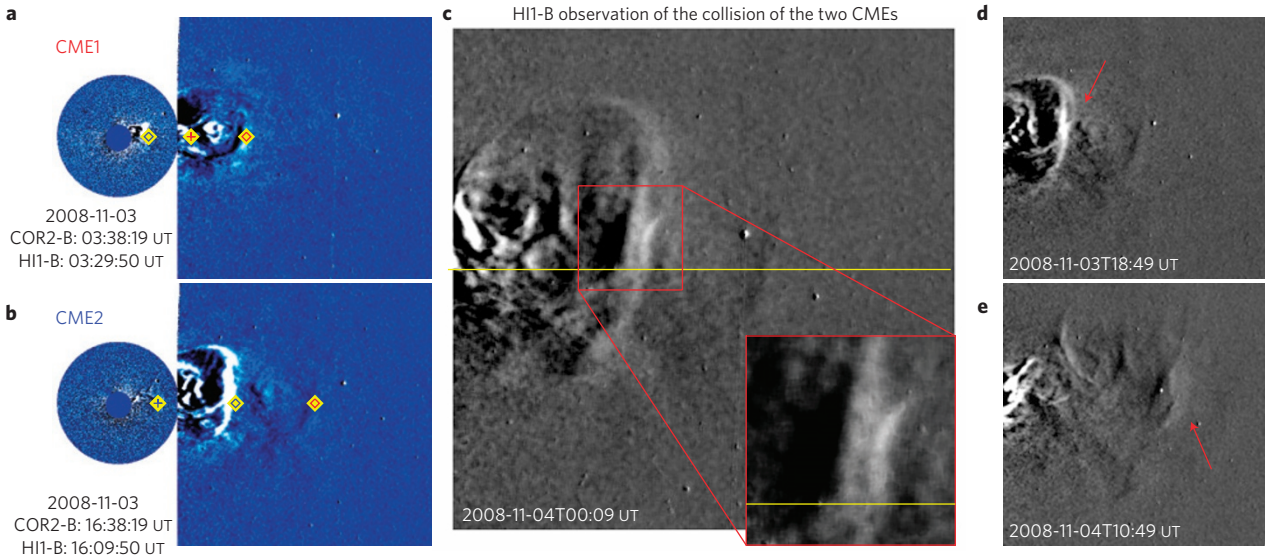

Figure 2 | The STEREO/SECCHI images of the two CMEs and their collision in the heliosphere. a,**b**, Running-difference images showing CME1 and CME2. The red diamond and plus symbols mark the front and rear edges of CME1, respectively, and the blue symbols are for CME2. **c**, The running-difference image of HI1-B showing the collision of the two CMEs. **d**,**e**, The beginning and end of the collision; the red arrows indicate the collision region.

Being faster than CME1, CME2 finally caught up and collided with CME1. This phenomenon was clearly recorded by HI1 onboard STEREO-B, referred to as HI1-B from here. On the basis of the HI1-B images, we can see that the distance between the front edge of CME2 and the rear edge of CME1 became smaller and smaller. The apparent touch of the two CMEs began at approximately 18:49 UT on 3 November 2008, which was registered as a significant enhancement of the brightness around an arc-shaped structure (Fig. 2d). We call the brightness-enhanced region a collision region, and the arc structure is the core of the region. As the arc structure is caving into CME2, the brightness enhancement is not simply due to superposition of the two CMEs, but probably the result of a soft object colliding with a hard object. In fact, if the two CMEs did not collide, the kinetic evolution of CME1 cannot be explained only by solar wind acceleration (see Supplementary Section S11). The brightened arc structure stayed visible for about 7 h with the most clear appearance at around 00:09 UT on 4 November (Fig. 2c). The whole collision region remained brightened much longer until 10:49 UT on 4 November 2008 (Fig. 2e). It seems that the entire collisional process of such large-scale magnetized plasmoids is similar to that of elastic balls, which includes a pre-collision phase, a compression phase, a restitution phase and a post-collision phase. We think that the appearance and disappearance of the visible arc structure define the start and the end of the compression phase, respectively, and the complete disappearance of the brightened region between the two CMEs marks the end of the restitution phase, that is, the end of the collision between them. Movies are available in the Supplementary Information.

Tracking and dynamics of the two CMEs in the heliosphere

To analyse the dynamics of the CMEs and their collision, a time-elongation map, known as a J-map[17,36–38], is constructed. To facilitate the comparison between imaging data and *in situ* data at 1 AU, a 64-pixel-wide slice is placed along the ecliptic plane in the running-difference images from COR2, HI1 and HI2 onboard STEREO-B to produce the J-map (Fig. 3). A bright–dark alternating track from the lower-left to the upper-right usually indicates a bright structure moving away from the Sun. The two vertical dotted green lines mark the start and end times of the collision.

The front edges of CME1 and CME2 are distinct in the J-map as marked by the red and blue diamonds, respectively. They are the same points marked by the red and blue diamond in Fig. 2a,b. The rear edges of the two CMEs are not clear in the J-map. To find out where the tracks of the rear edges of the two CMEs are, we directly

identify their rear edges in coronagraph images as done in Fig. 2a,b, and then dot them back to the J-map as shown by the red and blue plus symbols, respectively. Note that the significant track between the red diamond and the plus symbols does not correspond to the CME1's rear edge but to its bright core.

The elongation angle of a given feature in the J-map can be converted to the heliocentric distance under some assumptions[17,38–40]. An often used assumption is to approximate a CME as a sphere[21,32]. By further assuming that the front and rear edges recorded in the J-map are the points of tangency determined by the circular cross-section of the CME in the ecliptic plane and the observer STEREO-B, we get the heliocentric distance of the CME centre, d, its radius, r, and their projected components on the ecliptic plane, d_p and r_p, in terms of the heliocentric distance, l, of STEREO-B, the elongation angles, ε_F and ε_R, of the CME front and rear edges, and the latitude, θ, and longitude, φ, of the CME centre. The detailed derivation can be found in Supplementary Section S4. Owing to the presence of the solar wind stretching effect, a CME might become pancake shaped even if it was initially spherical[41,42]. The HI1 imaging data suggest that the effect is significant for CME2, but not for CME1. Thus, a small correction is made to CME2 to reduce the effect (see Supplementary Section S5).

With the aid of the graduated cylindrical shell model[43,44], the latitude, θ, and longitude, φ, of the two CME centres can be obtained from COR2 images. It is found that both CMEs propagated almost radially with a nearly constant longitude and latitude in the COR2 field of view[35], which are listed in Table 1 (see Supplementary Sections S2 and S3 for details). As the interplanetary magnetic field and solar wind density get weaker and lower, respectively, farther away from the Sun, it is reasonable to assume that they would keep their propagation directions in the HI1 field of view until the collision. The results given by the model suggest that both CMEs propagated between the Sun–Earth line and the Sun–STEREO-A line with CME1 closer to the latter line and CME2 closer to the former, which is in agreement with the previous study[35].

Figure 4 shows d and r as a function of time for both CMEs. As the front and rear edges of the CMEs are more or less diffused, a reasonable error of $\pm 5\%$ in the determination of the elongation angle of the CME front and rear edges is considered. The resultant uncertainties of d and r are indicated by the error bars in Fig. 4. By applying the linear fitting to d and r with these uncertainties taken into account, we get the propagation speed v_c and expansion speed v_e of the two CMEs, as well as their components in the ecliptic plane, v_p and v_{ep}. A 2-σ uncertainty of the speeds derived from the linear fitting is applied in the following analysis. The excellent consistency between the fitting lines and the data points suggests that the two CMEs experienced a nearly constant-speed propagation and expansion in the heliosphere before they met, although a very weak acceleration can be seen for CME1. It should be noted that the uncertainties of CMEs' directions may cause extra uncertainties of CMEs' speeds, and therefore the final values of the uncertainties of CMEs' speeds (see v_c and v_e listed in Table 1) are larger than those given in Fig. 4. Besides, although the front edge of CME2 perhaps travelled faster than the background solar wind, observations suggest that it did not drive an evident shock ahead (see Supplementary Section S12).

Furthermore, in the opposite manner, we derive the elongation angle-time curves from the above results, and plot them on the J-map as white dashed lines in Fig. 3. These white dashed lines are also extrapolated to the post-collision phase. It is found that the fitting lines match the observed tracks very well before the collision, but begin to deviate from the tracks at the beginning of the collision (particularly note the tracks of the two CMEs' front edges). Such deviations mean that the collision between the two CMEs must have significantly changed their propagation directions and/or speeds.

As an attempt, we might as well treat the CMEs approximately as a expanding ball in the collision. The situations of the two CMEs at the time of touching have been sketched in Fig. 1b. It is a collision in three-dimensional space, which should push CME1 closer to the Sun–STEREO-A line in the ecliptic plane and CME2 further away from the ecliptic plane. Thus, it is expected that CME1 would be observed *in situ* by the instruments onboard STEREO-A whereas CME2 would be missed by the *in situ* instruments, which are all located in the ecliptic plane. The *in situ* data at 1 AU do suggest that only CME1 was observed as expected (see Supplementary Section S6 for more details). Its propagation and expansion speeds at 1 AU were about 342 and 30 km s^{-1}, respectively. The increased propagation speed is consistent with our conjecture that CME1 was accelerated by the collision. The expansion speed is very close to that derived from the J-map. This fact allows us to reasonably assume that the expansion speed was recovered after the collision for both CMEs, although the expansion speed may vary greatly during the collision and CME2 was not locally observed at 1 AU.

Super-elastic collision and the energy exchange

For the case of two expanding elastic balls, not only will their collision result in a momentum exchange in the direction connecting the centroids of the two balls (referred to as the collision direction hereafter), but also their continuous expansion may cause their centroids to separate farther away. We define the approaching speed as the speed of the centroid of one ball relative to the other in the collision direction. Under the assumption that the expansion speeds remained unchanged before and after collision, the collision should be super-elastic if the sum of the expansion speeds of the two balls was larger than the approaching speed before the collision. Here we first show the results for the case of the CMEs' parameters given in Table 1, and then analyse the influence of the uncertainties.

According to the values listed in Table 1, we can derive that the latitude θ_C and longitude φ_C of the collision direction at the beginning of the collision, that is, the elevation angle and azimuthal angle in the heliocentric coordinate system, are about $-10°$ and $57°$, respectively. By resolving the propagation velocity vectors into the components parallel, $v_\parallel$, and perpendicular, $v_\perp$, to the collision direction (see Supplementary Section S7), we find that the values of $v_\parallel$ of the two CMEs were 205 and 237 km s^{-1}, respectively (listed in Table 1), which give an approaching speed of about 32 km s^{-1}. The sum of the expansion speeds of the two CMEs was about 117 km s^{-1}, much larger than the approaching speed. Hence a super-elastic collision is expected.

The conservation of momentum requires $m_1 v_{1\parallel} + m_2 v_{2\parallel} = m_1 v'_{1\parallel} + m_2 v'_{2\parallel}$, where m_1 and m_2 are the mass of CME1 and CME2, respectively, and the prime symbol denotes the parameters after the collision. Here, we approximately treat the collision phase including the compression and restitution phases as a black box, and adopt parameters of the two CMEs before (after) the collision for the first (second) half-period of the collision phase. The influence of this simplification on our final result is not significant (see Supplementary Section S8).

The mass of a CME can be calculated from calibrated coronagraph images[45]. For CME1 and CME2, the derived masses based on COR2-B observations are about 1.8×10^{12} kg and 1.2×10^{12} kg, respectively. The Thomson scattering and projection effects have been corrected[46,47]. The mass ratio of CME1 to CME2 is about 1.5. Hence, for any given coefficient of restitution e, that is, $v'_{2\parallel} - v'_{1\parallel}/v_{1\parallel} - v_{2\parallel}$, the velocities of the two CMEs after the collision can be obtained (see Supplementary Section S7) as well as the expected tracks of the front and rear edges of both the CMEs in the J-map. In fact, our calculation suggests that, no matter which value of the mass ratio we choose, the super-elastic nature of the collision, which will be seen below, does not change (see Supplementary Section S9).

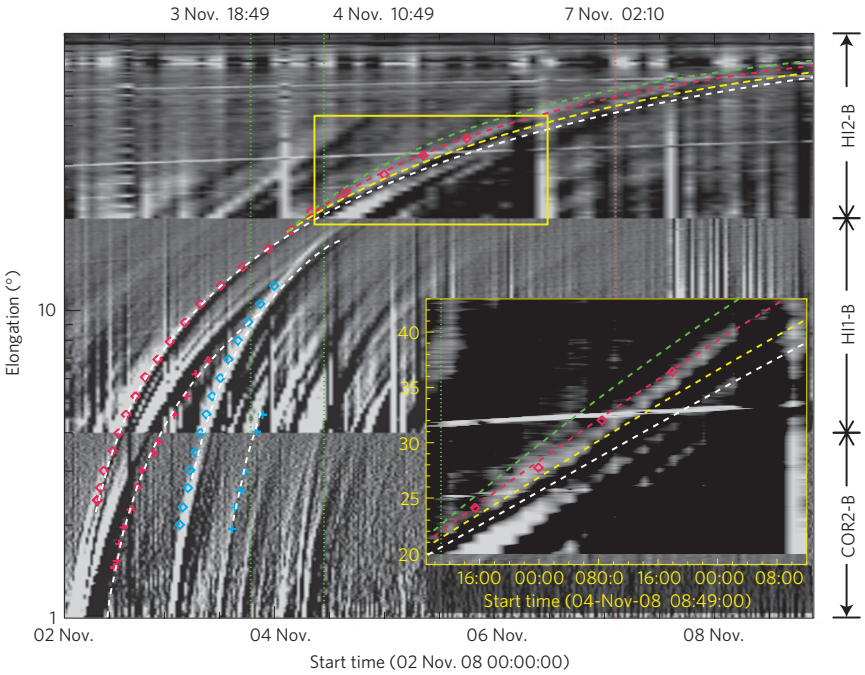

Figure 3 | The time-elongation map from 2 to 9 November 2008 constructed on the basis of the running-difference images from STEREO-B. The diamonds and plus symbols show the front and rear edges of the CMEs, respectively. The two vertical dotted green lines indicate the start and end of the collision. The red vertical line marks the arrival time of CME1 at STEREO-A. The region enclosed by the yellow rectangle is shown at a higher magnification in the lower-right corner. The colour-coded dashed lines are the predicted tracks.

Table 1 | The parameters of the two CMEs before and after the collision.

Parameters derived from observations

	θ	φ	v_c	v_e
CME1	6±2	28±10	243^{+25}_{-16}	43^{+16}_{-15}
CME2	16±2	8±10	407^{+102}_{-74}	74^{+65}_{-51}

Second-level derived parameters

	v_p	v_{ep}	θ_C	φ_C	$v_\perp$	$v_\parallel$	$v'_\parallel$	v'_c	v'_p	v'_{ep}	$\Delta\theta_v$	$\Delta\varphi_v$	$\Delta E/E$	$\Delta E_t/E_t$	e
CME1	241	36	−10	57	130	205	288	316	316	41	−4	7	68%	6.6%	5.4
CME2	392	26			332	237	116	351	325	N/A*	6	−16	−25%		

θ and φ are the CME's latitude and longitude. v_c and v_e are the propagation and expansion speed of a CME, derived from the J-map by assuming the CME is a sphere (see Supplementary Sections S4 and S5). v_p and v_{ep} are the average values of the components of v_c and v_e in the ecliptic plane, respectively. θ_C and φ_C are the latitude and longitude of the collision direction (see Supplementary Fig. S7). $v_\perp$ and $v_\parallel$ are the components of the CME velocity perpendicular and parallel to the collision direction, respectively. The superscript prime denotes the parameters after the collision. $\Delta\theta_v$ and $\Delta\varphi_v$ are the change of the CME velocity. $\Delta E/E = (E' - E)/E$ is the percentage of the kinetic energy changed, and E_t is the sum of the kinetic energy of the two CMEs. All of the angles in the table are in units of degrees, and all of the speeds are in units of kilometres per second. Here, only the uncertainties of θ, φ, v_c and v_e are listed, and the uncertainties of speeds have included the uncertainties in the CMEs' directions. The uncertainties of the second-level derived parameters are not listed, but are all taken into account in our analysis. *After the collision, CME2 left the ecliptic plane, and thus there is no available component of expansion speed in the ecliptic plane.

In the J-map, only the track of the front edge of CME1 is still identifiable after the collision. Thus, we repeatedly adjust the value of e to find the best match for the observed track. For the parameters listed in Table 1, the red dashed line starting at the middle of the collision in Fig. 3 shows the best predicted track of the front edge of CME1, which gives $e = 5.4$. As a comparison, the tracks for e equal to 1 and 10 are presented by the yellow and green dashed lines, respectively. A zoomed-in image in the lower-right corner of Fig. 3 presents the details. Obviously, the tracks predicted by both the yellow and green dashed lines get worse. $e = 1$ indicates a perfect elastic collision, but the yellow line is obviously lower than the observed track indicated by the red diamond. The $0 < e < 1$ tracks predicted by our calculation would be located even lower.

As summarized in Table 1, through the collision, CME1 was deflected southwestward and its propagation speed increased from 243 km s^{-1} to about 316 km s^{-1}, whereas CME2 was deflected northeastward and its speed decreased from 407 to 351 km s^{-1}. The *in situ* propagation speed of CME1 was about 40 km s^{-1} larger than the derived post-collision speed of CME1. This is probably due to the continuous acceleration by the solar wind. According to the result, the two CMEs were separating after the collision (see Supplementary Section S10 for a preliminary discussion). It is worth noting that CME2 is completely above the ecliptic plane after the collision. Therefore, it is not surprising that no counterpart of CME2 was detected by *in situ* instruments located in the ecliptic plane. Furthermore, the kinetic energy of CME1 (the contribution from the CME expansion has been taken into account) is found

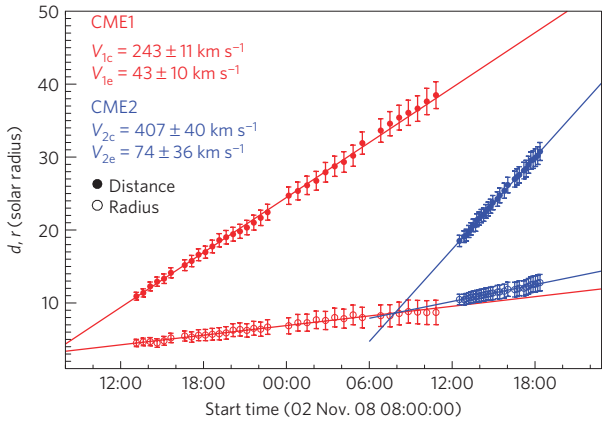

Figure 4 | The heliocentric distance *d* and the radius *r*, in units of solar radius, of the two CMEs as functions of time for the case that θ and φ of CME1 are 6° and 28°, respectively, and those of CME2 are 16° and 8°, respectively. The error bars are derived from the 5% uncertainty in the elongation angle. The speeds are obtained by linear fitting with the error bars taken into account, and a 2-σ uncertainty is chosen, which makes the confidence level greater than 95%.

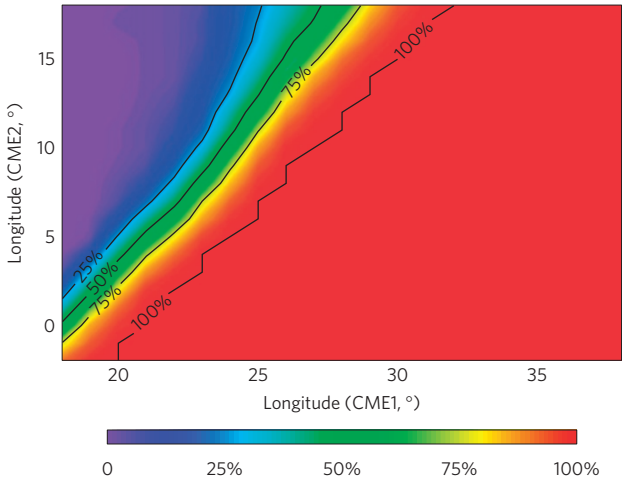

Figure 5 | Likelihood of super-elastic collision calculated by varying the CMEs' longitudes and speeds within their uncertainties. .

to increase by about 68%, whereas that of CME2 decreased by about 25%. As a whole, the system gained about 6.6% kinetic energy during the collision.

The influence of large uncertainties, that is, those in the CMEs' longitudes and velocities as listed in Table 1, is further examined. We sample the longitudes of the two CMEs at 1° within the 10° uncertainty. For each possible pair of longitudes we consider a combination of five propagation speeds, $[v_c \pm \Delta_{vc}, v_c \pm 0.5\Delta_{vc}, v_c]$, for either of both CMEs and five expansion speeds, $[v_e \pm \Delta_{ve}, v_e \pm 0.5\Delta_{ve}, v_e]$, for CME1, which constitute 125 cases. Here, Δ_{vc} and Δ_{ve} are the uncertainties in the CME speeds. For each case we are able to obtain a value of e and the change of the total kinetic energy. The likelihood of super-elastic collision for each longitude pair is therefore calculated. Figure 5 presents the result. Most areas show a strong likelihood of super-elastic collision. Specifically, 72.6% are more than 75% likely, and 63.0% are 100% likely, to experience a super-elastic collision. In contrast, as few as 6.3% combinations are definitely non-super-elastic. Overall, it is 72.8% likely for the collision to be super-elastic.

Source of kinetic energy gain

The source of the net kinetic energy gain and the mechanism of the energy conversion are key issues for super-elastic collisions. The divergent configuration of solar wind implies that the internal pressure of a CME is always stronger than the external pressure when it moves away from the Sun, which is the main cause of the CME expansion. In this process, the magnetic and thermal energies of the CME are continuously dissipated[48,49]. It could be estimated that, for a typical CME at 1 AU with a magnetic field strength of 10 nT, temperature of 10^5 K, density of 5 cm^{-3} and velocity of 500 km s^{-1}, the magnetic and thermal energy density is about 6% of the kinetic energy density. The percentage will be much higher when the CME is closer to the Sun. Thus, the magnetic and thermal energy of CMEs should be sufficient to provide a ~6.6% increase in the kinetic energy in the super-elastic collision, and the persistent expansion of CMEs may provide the way for the magnetic/thermal energy to convert into kinetic energy.

Besides, the detailed interacting process may also be important in determining the nature of the collision. An anti-correlation between the impact velocity and the coefficient of restitution was reported in collisions among ice particles of Saturn's B ring[1] and granular materials[50]. Experiments and simulations on granular materials and nanoclusters have further shown that the collision between a hard sphere and a soft plate tends to be super-elastic[2,4,5]. These imply that super-elastic collision requires sufficient interaction time and touching area for momentum exchange and energy conversion. In our case, the compression and restitution phases lasted about 16 h, during which a clear arc-shaped structure stayed visible for about 7 h. These phenomena suggest that the two CMEs had sufficient time and a sufficiently large touching area to convert magnetic/thermal energy into kinetic energy. It is worthy of further investigation to examine whether a similar anti-correlation applies to CME collisions, that is, whether a larger coefficient of restitution corresponds to a lower impact velocity.

Although in granular physics, rotational motion and thermal fluctuation have been considered the possible mechanism for the increased kinetic energy[2–5], they are probably not suitable for CME collisions. First, there is no evidence that plasma within a CME undergoes a significant rotation in interplanetary space. Second, CMEs are large-scale structures with huge mass and thus the thermal fluctuation of microscopic particles should not be able to affect the macroscopic behaviour of CMEs.

The good match between the predictions of the simplest collision model and the observations suggests that such large-scale magnetized plasmoids could be simplified as balls instead of using complicated magnetohydrodyanmics or plasma kinetic theories in studying their collision. The collision may be super-elastic, through which the system gains kinetic energy from the magnetic/thermal energy of CMEs. Of course, the process and consequence might be different if significant reconnection occurs in the collision region. This will be another issue.

Received 3 March 2012; accepted 3 September 2012; published online 7 October 2012

References

1. Bridges, F. G., Hatzes, A. & Lin, D. N. C. Structure, stability and evolution of Saturn's rings. *Nature* **309,** 333–335 (1984).
2. Louge, M. Y. & Adams, M. E. Anomalous behavior of normal kinematic restitution in the oblique impacts of a hard sphere on an elastoplastic plate. *Phys. Rev. E* **65,** 021303 (2002).
3. Kuninaka, H. & Hayakawa, H. Simulation of cohesive head-on collisions of thermally activated nanoclusters. *Phys. Rev. E* **79,** 031309 (2009).
4. Saitoh, K., Bodrova, A., Hayakawa, H. & Brilliantov, N. V. Negative normal restitution coefficient found in simulation of nanocluster collisions. *Phys. Rev. Lett.* **105,** 238001 (2010).
5. Kuninaka, H. & Hayakawa, H. Anomalous behavior of the coefficient of normal restitution in oblique impact. *Phys. Rev. Lett.* **93,** 154301 (2004).
6. Smith, C. E. & Liu, P-P. Coefficients of restitution. *J. Appl. Mech.* **59,** 963–969 (1992).

7. Calsamiglia, J., Kennedy, S. W., Chatterjee, A., Ruina, A. & Jenkins, J. T. Anomalous frictional behavior in collisions of thin disks. *J. Appl. Mech.* **66,** 146–152 (1999).
8. Lepping, R. P., Jones, J. A. & Burlaga, L. F. Magnetic field structure of interplanetary magnetic clouds at 1 AU. *J. Geophys. Res.* **95,** 11957–11965 (1990).
9. Yashiro, S. *et al.* A catalog of white light coronal mass ejections observed by the soho spacecraft. *J. Geophys. Res.* **109,** A07105 (2004).
10. Burlaga, L. F., Plunkett, S. P. & St Cyr, O. C. Successive CMEs and complex ejecta. *J. Geophys. Res.* **107,** 1266 (2002).
11. Wang, Y. M., Wang, S. & Ye, P. Z. Multiple magnetic clouds in interplanetary space. *Sol. Phys.* **211,** 333–344 (2002).
12. Wang, Y. M., Ye, P. Z. & Wang, S. Multiple magnetic clouds: Several examples during March–April, 2001. *J. Geophys. Res.* **108,** 1370 (2003).
13. Wang, Y. M., Ye, P. Z., Wang, S. & Xue, X. H. An interplanetary cause of large geomagnetic storms: Fast forward shock overtaking preceding magnetic cloud. *Geophys. Res. Lett.* **30,** 1700 (2003).
14. Farrugia, C. & Berdichevsky, D. Evolutionary signatures in complex ejecta and their driven shocks. *Ann. Geophys.* **22,** 3679–3698 (2004).
15. Wang, Y. *et al.* Impact of the major coronal mass ejections on geo-space during September 7–13, 2005. *Astrophys. J.* **646,** 625–633 (2006).
16. Harrison, R. A. *et al.* Two years of the STEREO heliospheric imagers. Invited review. *Sol. Phys.* **256,** 219–237 (2009).
17. Liu, Y. *et al.* Geometric triangulation of imaging observations to track coronal mass ejections continuously out to 1 AU. *Astrophys. J.* **710,** L82–L87 (2010).
18. Liu, Y., Luhmann, J. G., Bale, S. D. & Lin, R. P. Solar source and heliospheric consequences of the 2010 April 3 coronal mass ejection: A comprehensive view. *Astrophys. J.* **734,** 84 (2011).
19. Gopalswamy, N., Yashiro, S., Kaiser, M. L., Howard, R. A. & Bougeret, J. L. Radio signatures of coronal mass ejection interaction: Coronal mass ejection cannibalism? *Astrophys. J.* **548,** L91–L94 (2001).
20. Shen, C., Wang, Y., Ye, P. & Wang, S. Enhancement of solar energetic particles during a shock-magnetic cloud interacting complex structure. *Sol. Phys.* **252,** 409–418 (2008).
21. Lugaz, N., Vourlidas, A. & Roussev, I. I. Deriving the radial distances of wide coronal mass ejections from elongation measurements in the heliosphere application to CME–CME interaction. *Ann. Geophys.* **27,** 3479–3488 (2009).
22. Liu, Y. D. *et al.* Interactions between coronal mass ejections viewed in coordinated imaging and *in situ* observations. *Astrophys. J.* **746,** L15 (2012).
23. Martínez Oliveros, J. C. *et al.* The 2010 August 01 type II burst: A CME – CME interaction, and its radio and white-light manifestations. *Astrophys. J.* **748,** 66 (2012).
24. Temmer, M. *et al.* Characteristics of kinematics of a coronal mass ejection during the 2010 August 1 CME–CME interaction event. *Astrophys. J.* **749,** 57 (2012).
25. Gonzalez-Esparza, A., Santillán, A. & Ferrer, J. A numerical study of the interaction between two ejecta in the interplanetary medium: one- and two-dimensional hydrodynamic simulations. *Ann. Geophys.* **22,** 3741–3749 (2004).
26. Schmidt, J. & Cargill, P. A numerical study of two interacting coronal mass ejections. *Ann. Geophys.* **22,** 2245–2254 (2004).
27. Wang, Y., Zheng, H., Wang, S. & Ye, P. MHD simulation of the formation and propagation of multiple magnetic clouds in the heliosphere. *Astron. Astrophys.* **434,** 309–316 (2005).
28. Lugaz, N., Manchester, W. B. IV & Gombosi, T. I. Numerical simulation of the interaction of two coronal mass ejections from Sun to Earth. *Astrophys. J.* **634,** 651–662 (2005).
29. Hayashi, K., Zhao, X-P. & Liu, Y. MHD simulation of two successive interplanetary disturbances driven by cone-model parameters in IPS-based solar wind. *Geophys. Res. Lett.* **33,** 20103 (2006).
30. Xiong, M., Zheng, H., Wu, S. T., Wang, Y. & Wang, S. Magnetohydrodynamic simulation of the interaction between two interplanetary magnetic clouds and its consequent geoeffectiveness. *J. Geophys. Res.* **112,** A11103 (2007).
31. Xiong, M., Zheng, H. & Wang, S. Magnetohydrodynamic simulation of the interaction between two interplanetary magnetic clouds and its consequent geoeffectiveness: 2. Oblique collision. *J. Geophys. Res.* **114,** A11101 (2009).
32. Shen, F. *et al.* Three-dimensional MHD simulation of two coronal mass ejections' propagation and interaction using a successive magnetized plasma blobs model. *J. Geophys. Res.* **116,** A09103 (2011).
33. Howard, R. A. *et al.* Sun earth connection coronal and heliospheric investigation (SECCHI). *Space Sci. Rev.* **136,** 67–115 (2008).
34. Kaiser, M. L. *et al.* The stereo mission: An introduction. *Space Sci. Rev.* **136,** 5–16 (2008).
35. Kilpua, E. K. J. *et al.* STEREO observations of interplanetary coronal mass ejections and prominence deflection during solar minimum period. *Ann. Geophys.* **27,** 4491–4503 (2009).
36. Sheeley, N. R. Jr, Walters, J. H., Wang, Y-M. & Howard, R. A. Continuous tracking of coronal outflows: Two kinds of coronal mass ejections. *J. Geophys. Res.* **104,** 24739–24768 (1999).
37. Davies, J. A. *et al.* A synoptic view of solar transient evolution in the inner heliosphere using the heliospheric imagers on STEREO. *Geophys. Res. Lett.* **36,** L02102 (2009).
38. Liu, Y. *et al.* Reconstructing coronal mass ejections with coordinated imaging and *in situ* observations: Global structure, kinematics, and implications for space weather forecasting. *Astrophys. J.* **722,** 1762–1777 (2010).
39. Lugaz, N. Accuracy and limitations of fitting and stereoscopic methods to determine the direction of coronal mass ejections from heliospheric imagers observations. *Sol. Phys.* **267,** 411–429 (2010).
40. Lugaz, N. *et al.* Determining the azimuthal properties of coronal mass ejections from multi-spacecraft remote-sensing observations with STEREO SECCHI. *Astrophys. J.* **715,** 493–499 (2010).
41. Riley, P. & Crooker, N. U. Kinematic treatment of coronal mass ejection evolution in the solar wind. *Astrophys. J.* **600,** 1035–1042 (2004).
42. Liu, Y., Richardson, J. D., Belcher, J. W. & Kasper, J. C. Constraints on the global structure of magnetic clouds: Transverse size and curvature. *J. Geophys. Res.* **111,** A12S03 (2006).
43. Thernisien, A., Howard, R. & Vourlidas, A. Modeling of flux rope coronal mass ejections. *Astrophys. J.* **652,** 763–773 (2006).
44. Thernisien, A. Implementation of the graduated cylindrical shell model for the three-dimensional reconstruction of coronal mass ejections. *Astrophys. J. Suppl. Ser.* **194,** 33 (2011).
45. Vourlidas, A., Subramanian, P., Dere, K. P. & Howard, R. A. Large-angle spectrometric coronagraph measurements of the energetics of coronal mass ejections. *Astrophys. J.* **534,** 456–467 (2000).
46. Hundhausen, A. J. Sizes and locations of coronal mass ejections—SMM observations from 1980 and 1984–1989. *J. Geophys. Res.* **98,** 13177–13200 (1993).
47. Vourlidas, A. & Howard, R. A. The proper treatment of coronal mass ejection brightness: A new methodology and implications for observations. *Astrophys. J.* **642,** 1216–1221 (2006).
48. Kumar, A. & Rust, D. M. Interplanetary magnetic clouds, helicity conservation, and current-core flux-ropes. *J. Geophys. Res.* **101,** 15667–15684 (1996).
49. Wang, Y., Zhang, J. & Shen, C. An analytical model probing the internal state of coronal mass ejections based on observations of their expansions and propagations. *J. Geophys. Res.* **114,** A10104 (2009).
50. Hayakawa, H. & Kuninaka, H. Theory of the inelastic impact of elastic materials. *Phase Transit.* **77,** 889–909 (2004).

Acknowledgements

We acknowledge the use of data from the SECCHI, IMPACT, PLASTIC and WAVES instruments on STEREO, LASCO on SOHO and WAVES on WIND. STEREO is the third mission in NASA's Solar Terrestrial Probes programme, and SOHO is a mission of international cooperation between ESA and NASA. Y.W. also thanks N. Lugaz for some valuable discussion. This work is supported by grants from the 973 key project 2011CB811403, NSFC 41131065, 40904046, 40874075 and 41121003, CAS the Key Research Program KZZD-EW-01, 100-talent program, KZCX2-YW-QN511 and start-up fund, and MOEC 20113402110001 and the fundamental research funds for the central universities.

Author contributions

Y.W. designed the analysis of the collision and performed the theoretical derivations. C.S. found this event and carried out the data processing and calculations. S.W. gave constructive suggestions on the analysis of the collision. Y.L. gave some advice on the construction of the J-map and interpretation of the elongation angle. B.M. carried out the literature investigation and provided valuable additions. A.V. calculated the masses of the CMEs and gave many valuable suggestions. R.L. and P.Y. participated in the discussion and gave many suggestions. J.L. and Z.Z. made a contribution to the data analysis.

Additional information

Supplementary information is available in the online version of the paper. Reprints and permissions information is available online at www.nature.com/reprints.

Correspondence and requests for materials should be addressed to Y.W.

Competing financial interests

The authors declare no competing financial interests.